Influence of high-temperature solution treatments on mechanical properties of an Al-Si-Cu aluminum alloy

Toda, Hiroyuki
Toyohashi University of Technology

Nishimura, Takanori
Toyohashi University of Technology

Uesugi, kentaro
Japan Synchrotron Radiation Research Institute(JASRI)

Suzuki, Yoshio
Japan Synchrotron Radiation Research Institute(JASRI)

他

出版情報：Acta Materialia. 58 (6), pp.2014-2025, 2010-04-01. Elsevier
バージョン：
権利関係：

Influence of high-temperature solution treatments on mechanical properties of an Al-Si-Cu aluminum alloy

Hiroyuki Toda[a], Takanori Nishimura[a], Kentaro Uesugi[b], Yoshio Suzuki[b], Masakazu Kobayashi[a]

[a] Department of Production Systems Engineering, Toyohashi University of Technology, Toyohashi, Aichi 441-8580, Japan (e-mail: toda@pse.tut.ac.jp, tel: +81-532446697, fax: +81-532446690 (H. Toda))

[b] Japan Synchrotron Radiation Research Institute, 1-1-1, Kouto, Mikazuki-cho, Sayo-gun, Hyogo 679-5198 Japan

Abstract

It has been demonstrated that the strength of an Al-Si-Cu alloy is maximized by high-temperature solution treatment at 807 K, which is approximately 16 K higher than the ternary eutectic temperature. The dual-energy K-edge subtraction imaging technique has been employed to obtain the spatial distribution of copper and its change during its solution treatment in 3D quantitatively, providing interpretations of the improved mechanical properties in terms of age-hardenability and its spatial variation. It has been also confirmed that the occurrence of incipient local melting and the accompanying growth of micropores adjacent to the melt regions lead to fractures caused by these defects. However, it can be inferred that the positive effects can outweigh the negative effects even above the eutectic temperature, thereby realizing the maximum strength at such relative high temperature levels.

Keywords: Cast Aluminum Alloys; High-Temperature Solution Heat Treatment; X-ray Tomography; K-edge Subtraction Imaging; Chemical Concentration Mapping

1. Introduction

When more than one soluble phase is formed during solidification, as found with Al-Si-Cu-Mg and Al-Zn-Cu-Mg alloys, it can be readily supposed that phases with lower melting points are melted locally during subsequent heating. In practical aluminum alloys, a uniform solute-atom concentration is not realized during solidification owing to non-equilibrium solidification [1]. Therefore, in most alloy systems, segregation also renders the alloys prone to the formation of eutectic compounds with a low melting point. This means that the homogenization and solution heat treatment temperatures can sometimes exceed the final solidification temperature at which eutectic compounds are formed during solidification. If the compounds do not dissolve before the final solidification temperature is reached during heating, local melting occurs during the heat treatments. In addition, other local melting mechanisms, which can happen even without segregation, have been reported for dilute Al-Mg-Si [2] and Al-Zn-Mg [3] alloys. For these reasons, industrial solution heat treatments are performed well below eutectic solidus temperatures. For example, a typical solution heat treatment temperature of 773 to 778 K has been specified for an Al-6Si-3.5Cu alloy, which is designated as A319 in ANSI or AC2B in JIS. The temperatures are roughly 50 K lower than the eutectic solidus temperature of the Al-6Si-3.5Cu alloy.

It might be reasonable and efficient to hold a material at a sufficiently high temperature long enough to allow constituents to dissolve into a solid solution during homogenization and solution heat treatments. Given that diffusion is accelerated as the temperature is increased, it would be natural to attempt to maximize the solution heat treatment temperature. Shimizu et al. have demonstrated that toughness is maximized when an AC2B alloy is solution-heat-treated at 798 K [4]. They attributed the toughness enhancement to the spherodization of eutectic Si particles, the dissolution of non-equilibrium Cu bearing compounds and the refinement of needle-shaped Fe-bearing compounds. Koga et al. have also shown that the tensile strength of an Al-7.2Si-0.37Mg alloy was maximized under a solution treatment condition of 843 K – 0 ks [5]. They also attributed this to the spherodization and coarsening of eutectic silicon particles. Irinouchi et al. have investigated the effects of solution treatment temperature and time (813-843 K/0.9-18 ks) on the mechanical properties of an Al-6.7Si-0.31Mg alloy [6]. It has been clarified that a solution treatment at 833 K for 1.8 ks results in superior mechanical properties including 16 and 35 % increases in ultimate tensile strength and 0.2 % proof strength, respectively, together with a shorter solution treatment time (typically 1/10 of the standardized time). It has been confirmed with the X-ray tomography

technique that micropores and intermetallic compounds are grown during the solution treatment, thereby showing that the mechanical property degradation caused by further solution treatment might be attributable to these microstructural changes. Sokolowski et al. have attempted to increase the solution treatment temperature of A319 alloy to 788 K by introducing a preliminary solution treatment at 768 K [7].

It would be reasonable to assume that the positive effects of a high-temperature solution treatment are competent with its negative effects, and that the optimum condition is realized according to their trade-off relationship when the former exceeds the latter in terms of extent. For age-hardening aluminum alloys, the positive effects would consist of enhanced age-hardenability, homogeneization and the suppression of the brittle fracture of Si and intermetallic compound particles due to refinement and morphological modification. On the other hand, the negative effects are incipient melting and the resultant microstructural defects, such as micropores and brittle intermetallic compounds. Of these, the effects of the Si and intermetallic compound particles have been investigated relatively well, while the other factors remain poorly understood. Sampling a limited number of cross-sections using traditional metallographic observation might produce misleading information, especially for inhomogeneously and sparsely distributed microstructural features such as defects. To better understand the remaining negative effects, this study employed high-resolution three-dimensional (3D) imaging [8,9,10,11]. Also, the combination of this approach with K-edge subtraction imaging enables the visualization of local age-hardenability [12,13], thus providing a unique opportunity to analyze the positive effects quantitatively. This is clearly an improvement on the procedures described in the available literature on high-temperature solution treatment, which allow only qualitative and indirect evaluations.

2. Experiments

2.1 Sample preparation

Aluminum with a purity of 99.99% and Al-26%Si and Al-40%Cu mother alloys were used to prepare an Al-Si-Cu pure ternary alloy. The alloy was melted in ambient laboratory air, kept at 983 K for 1.8 ks, and then poured directly into a

steel mould about 153 × 270 × 100 mm in size that had been preheated at 473 K. Here, no modification was performed at all. The alloy cast had a chemical composition of 6.1 Si, 4.00 Cu, 0.09 Fe, 0.01 Ti, 0.0052 Ni, 0.0054 Ca and balance Al in mass %.

To determine the solution heat treatment temperatures, the differential scanning calorimetric (DSC) technique was employed with a sample mass of approximately 0.03 g. A specimen was heated in pure argon between room temperature and 873 K with a scan rate of 9 K per minute and a sampling interval of 1 s. In the DSC curve thus obtained, there were three endothermic peaks corresponding to ternary eutectic, unknown and binary eutectic reactions, respectively. In terms of the unknown second peak located at about 806 K, a much larger endotherm was observed in a practical AC2B alloy (Al-6.1Si-4.00Cu-0.17Fe-0.01Ti-0.01Mn-0.01Zn and balance Al in mass %) that has almost identical Si and Cu contents with more impurities. It is, therefore, reasonable to assume that the peak might be associated with the dissolution of some impurity-element-bearing phase. The extrapolated onset temperatures for the first and third peaks were located at 790.6 and 817.3 K, respectively. Four solution heat treatment temperatures of 773, 790, 807 and 824 K were selected considering the locations of the two peaks. 773 K is specified in the industrial standards. The samples were solution heat-treated for 0 – 36 ks in a salt bath, quenched in iced water, and then artificially aged for 18 ks at 433 K in an oil bath to provide a T6 temper condition. The interval between the quenching and the onset of the ageing treatment was controlled at 0.3 ks.

2.2 Tomographic imaging

X-ray tomography was performed using the undulator beamline BL20XU of the synchrotron radiation facility SPring-8. An experimental hutch is located about 245 m from the X-ray source in this beam line. First, an absorption spectrum was corrected in the 8.87 to 9.07 keV photon energy range around the Cu K-edge located at 8.977 keV as shown in Fig. 1. The monochromatized radiation was continuously monitored with ionization chambers. A 99.99 % copper thin film with a thickness of 5 μm was used for this measurement. 8.938 and 9.038 keV were chosen so that the imaging was performed outside the positions of near-edge features seen in Fig. 1. 20 keV was also used because it provides the optimum condition in terms of S/N ratio. A monochromatic X-ray beam produced by a liquid nitrogen-cooled Si (111) double crystal

monochromator was used for projection-type microtomography. An image detector was positioned 6 mm behind the sample, making the imaging system insensitive to phase modulation. The image detector consisted of a cooled 4000 (H) × 2624 (V) element CCD camera (effective pixel size of the camera: 5.9 μm), which was used in a 2 x 2 binning mode, a single crystal scintillator (Lu_2SiO_5:Ce) and a relay lens (×20). In total, 1500 radiographs, scanning 180 degrees, were obtained in 0.12-degree increments. The entire cross-section of the specimen and a region about 622 μm high were captured with the CCD camera.

Image slices were reconstructed from a series of projections based on the conventional filtered backprojection algorithm. The gray value in each dataset was calibrated unless otherwise noted so that the linear absorption coefficient of 0 ~ 350 cm^{-1} fell in an 8-bit grayscale range between 0 and 255. Isotropic voxels (a volume element in three-dimensional space) with 0.5 μm edges were achieved in the reconstructed slices. To estimate the volume of each micropore at sub-voxel accuracy, pentagonal facetted iso-intensity surfaces were computed from the volumetric data set using the conventional Marching Cubes algorithm [14]. The threshold value for obtaining binary images was chosen as the median between the linear absorption coefficient peaks of air and the aluminum matrix. To suppress inaccuracies originating from image noise, only micropores over 6.668 voxels in volume were counted as micropores in the quantitative analysis.

3. K-edge subtraction imaging

As seen in Fig. 1, the X-ray attenuation caused by the photoelectric absorption of Cu disappears, and the overall X-ray attenuation decreases by a factor of about 7 at the Cu K-edge. Since the energy resolution for the beam line $\Delta E/E \approx 10^{-4}$, where E is the X-ray energy, two consecutive tomographic images of an identical sample can be captured at 8.87 to 9.07 keV, completely dividing the two energies. The 3D image captured at the higher energy contains information provided by Compton scattering and photoelectric absorption from all the chemical elements in the sample, while the image captured at the lower energy contains almost identical information except for the absence of photoelectric absorption by Cu. Image registration was then performed for the two images with an accuracy of one voxel. Digital subtraction of the two images

resulted in the visualization of the Cu distribution in the sample. The measured mass absorption coefficients, μ_m^E, at X-ray energy, *E*, are given as follows;

$$\mu_m^{8.87} = C_{Cu}\mu_{m,Cu}^{8.87} + (1 - C_{Cu})\mu_{m,others}^{8.87} \quad (1)$$

$$\mu_m^{9.07} = C_{Cu}\mu_{m,Cu}^{9.07} + (1 - C_{Cu})\mu_{m,others}^{9.07} \quad (2)$$

where $\mu_{m,Cu}^E$ is the mass absorption coefficient at the X-ray energy, *E*, $\mu_{m,others}^E$ is the average mass absorption coefficient of the remaining elements at *E*, and C_{Cu} is the mass concentration of Cu in the entire material. The difference between $\mu_{m,others}^{8.87}$ and $\mu_{m,others}^{9.07}$ can be corrected using Victoreen's equation [15]. For example, the absorption coefficients of Al and Si vary by approximately 3 % from 93 to 90 and 103 to 100 cm^{-1}, respectively, between 8.87 and 9.07 keV. C_{Cu} can then be obtained as follows by eliminating $\mu_{m,others}^E$ from eqs. (1) and (2);

$$C_{Cu} = \frac{\Delta\mu\rho_{Cu}}{(\mu_{Cu}^{9.07} - \mu_{Cu}^{8.87})\rho_{alloy}} \quad (3)$$

where $\Delta\mu$ is obtained for each voxel by subtraction, μ_{Cu}^E is the linear absorption coefficient of Cu at *E*, and ρ is density. It has been confirmed that when the same setup is used, the detection limit for Cu is similar to that of the energy dispersive X-ray analysis in scanning electron microscopy (i.e., about 0.5 mass %), and a superior reproducibility of ±0.1 mass % is obtained [12].

Age-hardening precipitates, which appear during the aging treatment, are much smaller than the size of a voxel in this study. The age-hardening precipitates consist of θ"-Al_2Cu and θ'-Al_2Cu. Therefore, linear absorption coefficients measured at 9.07 keV can be expressed as follows;

$$\frac{\mu}{\rho} = \frac{\mu_\alpha w_\alpha}{\rho_\alpha} + \frac{\mu_{\theta'} w_{\theta'}}{\rho_{\theta'}} + \frac{\mu_{\theta''} w_{\theta''}}{\rho_{\theta''}} \quad (4)$$

where μ is the measured linear absorption coefficient. w_α, $w_{\theta''}$ and $w_{\theta'}$ are the mass fractions of the α-Al, θ" and θ' phases, respectively, and they satisfy $w_\alpha+w_{\theta''}+w_{\theta'}=1$. Measured linear absorption coefficients are corrected according to a correction line obtained with high-purity metals such as aluminum, magnesium and titanium to ensure the accuracy of the linear absorption coefficient measurement [12]. The subtraction also gives the following relationship for the Cu chemical concentration;

$$C_{\mathrm{Cu}} = w_\alpha C_{Cu}^{\alpha} + w_{\theta'} C_{Cu}^{\theta'} + w_{\theta''} C_{Cu}^{\theta''} \quad (5)$$

where C^{x}_{Cu} is the mass concentration of Cu in phase x. C^{α}_{Cu} is the equilibrium solubility limit of Cu in aluminum solution at room temperature (about 0.05 mass %). $C^{\theta''}_{\mathrm{Cu}}$ and $C^{\theta'}_{\mathrm{Cu}}$ are 0.440 and 0.541, respectively, according to the Al:Cu ratio in each unit lattice [16]. As previously reported, ρ_α for Al-0.05%Cu solid solution is 2.70 g/cm [3,17]. $\rho_{\theta''}$ and $\rho_{\theta'}$ can be calculated at 3.830 and 4.124 g/cm^3 from the lattice constant value and unit cell structure for each phase. μ_α, $\mu_{\theta''}$ and $\mu_{\theta'}$ values of 93.5, 551.5 and 697.6 cm^{-1} have been obtained. $\frac{\mu_{\theta''}}{\rho_{\theta''}}$ in eq. (4) is, therefore, approximately 15 % lower than that for $\frac{\mu_{\theta'}}{\rho_{\theta'}}$. This means that the measured Cu concentration can vary with the ratio of the θ" and θ' phases.

4. Mechanical properties and microstructural features after the high temperature solution treatments

4.1 Mechanical properties

Figure 2 shows the variations in Vickers hardness that occurred during solution heat treatments at various temperatures. Solid data were measured with a small applied load of 0.49 N within an α-Al phase. The indentation size was smaller than the size of the α-Al phase. On the other hand, open symbols were obtained with a load of 98 N, and represent the macroscopic strength of the whole material. During the solution treatments at 773 and 790 K, gradual increases in hardness are observed until a solution treatment time of 36 ks, while the hardness curves take the maxima before 10 ks at 807

and 824 K. The Vickers hardness values measured with a load of 98 N were always higher than those measured with a load of 0.49 N in the α-Al phase during the solution treatment at 773 K. This appears reasonable because rigid silicon particles, which have a higher elastic modulus than aluminum, are embedded in the Al-Si eutectic phases, which can effectively disturb the plastic flow of the aluminum matrix. The Vickers hardness measured within the α-Al phase increased significantly with increases in solution treatment temperature between 773 and 807 K, and then decreased greatly between 807 and 824 K. The peak hardness value measured within the α-Al phase for the 807 K-treated material is approximately 41 % higher than that obtained under the standard solution treatment condition complying with the industrial standard (i.e., 36 ks at 773 K). It is interesting to note that the Vickers hardness values measured within the α-Al phase exceed those for the whole material as a result of the solution treatment at 790 K, and the difference between them becomes significant for solution treatment at 807 K. It is also noteworthy that the peak hardness appears at 7.2 ks for the α-Al phase, while that for the whole material starts to decrease at 3.6 ks. In line with these tendencies, it can be presumed that the age-hardenability of the α-Al phase increases effectively with increases in solution treatment temperature up to 807 K, while that for the aluminum matrix in the Al-Si(-Cu) eutectic phase might be suppressed owing to certain negative factors that have developed with time at 807 and 824 K. In terms of the difference and orders between 98 and 0.49 N, the negative factors appear to exist even at 790 K, leading to a significant reduction in the hardness of the eutectic phase. In addition, the effects are pronounced after 807 K- 1.7 ks, and have significant effects even on the mechanical properties of the α-Al phase at 824 K.

Tensile tests were also performed for the heat treatment conditions used for Fig. 2. The ultimate tensile strength during solution heat treatments reached its maximum values before 20 ks, and sharp drops were observed after these peaks were reached, suggesting that the negative factor observed in Fig. 2 would be more pronounced under tension. A 12 % improvement was obtained for the optimum condition (i.e., 7.2 ks at 807 K) compared with the standard solution treatment complying with the industrial standard (i.e., 36 ks at 773 K), together with a 1/5 reduction in the time needed for the heat treatment. Even 0.9 ks at 807 K resulted in a strength value superior to the industrial standard, suggesting that there is a considerable advantage in reducing the time required to perform solutionizing.

4.2 Microstructural features

Figure 3 (a) and (b) show optical micrographs of the incipient melting observed at 807 and 824 K, respectively. A combination of blocky silicon particles, relatively coarse intermetallic compound particles and surrounding fine gray regions is observed in the images. Figure 3 (c) is a scanning electron microscope (SEM) image, representing a magnified view of the fine gray region shown in Fig. 3 (b). It is seen that the gray region consists of a sub-micron-sized eutectic microstructure. The fine light gray particles seen in Fig. 3 (c) were identified as Al_2Cu by energy dispersive X-ray analysis in the SEM. Figure 4 shows transmission electron micrographs for the two conditions where incipient melting was observed. The images were captured in the α-Al phase. It can be seen that the precipitates are coarse and sparsely distributed in the alloy solution-treated at 824 K for 7.2 ks, compared with that treated at 807 K for 7.2 ks. As regards the Al-Cu alloy, it has been reported that the reduction in Cu content gives rise to a change in phase at the peak aging from a predominant θ" phase with a small amount of θ' in Al-4.5%Cu to a θ' single phase in Al-2~3%Cu, suggesting qualitative agreement with Fig. 4 [18].

5. Tomographic observations and analyses

5.1 Positive effects of high-temperature solution treatment on mechanical properties

Four spherical regions with diameters of 40 μm and no visible particles were chosen for evaluating the local Cu concentration and its spatial variation. The regions are hereafter specified as A~D. The same four regions were tracked through the solution treatment at 807 K for 10.8 ks. The distribution profiles of the Cu concentration are shown in Fig. 5. In the as-cast condition, the average Cu concentration in each region varies within 2.1 ± 0.2 mass %. The peak height and the degree of broadening in each distribution also differ to some extent. During the first 1.8 ks, the mean Cu concentration and the fluctuation between the four regions increase greatly. This is probably due to the dissolution of the Cu-rich particles as shown later in Fig. 7. During the subsequent period of 5.4 ks, the mean Cu concentration gradually converges to approximately 4.5 mass %, and the distribution profiles become sharp and narrow. This concentration value seems to be

different from the macroscopically measured Cu content of 4.0 mass %, probably because of the small size of the tomography specimen. Complete homogenization is confirmed at 7.2 ks, where the distribution profiles and average Cu concentrations of the four regions are almost identical. It is interesting to note that the mean Cu concentration show a slight reduction again between 7.2 and 10.8 ks, together with the broadening of each distribution profile. The average concentration decreases by about 0.06 and 0.21 mass % in regions C and D, respectively, while a 0.09 mass % increase is observed in region B between 7.2 and 10.8 ks. These tendencies are consistent with the hardness variation shown in Fig. 3, where a significant increase in hardness until 1.8 ks is followed by a gradual increase until 7.2 ks, and then the hardness decreases slightly between 7.2 and 10.8 ks.

Figure 6 compares Cu concentration histograms for five selected solution treatment conditions that were measured using five different samples. The extent of homogenization appears to be different for the as-cast, 773 K – 36 ks and 807 K – 7.2 ks conditions, as reflected in the mechanical properties shown in Fig. 2. Further heat treatment at 807 K also induces broadening in the distribution profile, as shown in Fig. 5. The distribution profile of the Cu concentration becomes right-skewed at 807 K – 10.8 ks, compared with that obtained for 807 K - 7.2 ks, which is also seen in Fig. 5. This appears to be caused by the formation of fine Cu-rich particles in the sample. The sample treated at 824 K exhibits a reduction in Cu concentration together with broadening. As regards the Al-Cu alloy, it has been reported that a reduction in Cu content lengthens the time needed to reach peak aging as well as the reduction in peak hardness value, suggesting a qualitative agreement with the age-hardening curves obtained for the materials used [18].

5.2 Negative effects of high-temperature solution treatment on mechanical properties

5.2.1 Dispersion particles

Figure 7 shows eutectic regions in gray where the Cu concentration is higher than 8 %. Eutectic regions formed during solidification tend to disappear during the solution treatment of 0.9 ks at 807 K. The Cu concentration of 8 % was chosen so that the size of the eutectic regions became comparable to that obtained with an optical microscope, as shown by the gray region on the right side of Fig. 3 (a). Instead, rather spherical regions with smooth contours are observed at 0.9 ks,

and then gradually shrink over time. This is also confirmed in the summary of the quantitative image analyses shown in Fig. 8. Another noteworthy point is that the spherical shape can be associated with incipient melting. With the reduction in size and volume fraction, the Cu concentration decreases in each eutectic region, as shown in the magnified views in Fig. 9. In Fig. 9, red regions, which correspond to Cu concentrations higher than 30 mass %, are indicated by arrows. Cu-Al intermetallic compound particles that are much larger than the voxel size are embedded in some regions, which can be also confirmed from Fig. 3 (a) and (b). The high Cu concentration regions gradually disappear until 7.2 ks. Figure 8 shows that the volume fraction, size and number of eutectic regions decrease almost monotonously with time, while the sphericity begins to increase after 3.6 ks. It is worth noting that the number of high Cu regions suddenly increases by approximately 19 % between 7.2 and 10.8 ks, which can also be confirmed from Fig. 7 (f) and Fig. 9 (f). In these figures, relatively small particles are initiated where no particles were initially observed.

In Fig. 10, instantaneous melting is clearly seen at 824 K immediately after the onset of heating. Relatively large irregular regions with smooth surfaces (a few regions are seen in Fig. 10 (b)) and a number of small spherical regions might be traces of incipient melting. The irregular regions gradually coalesce, while the small spherical regions disappear with time.

5.2.2 Micropores

As seen in Figs. 7 and 10, micropores (shown in blue) are formed heterogeneously in eutectic regions. There is significant growth immediately after exposure to a temperature higher than ternary and binary eutectic temperatures, and this is summarized in Fig. 11. It can be inferred that micropore growth might be attributable to the creep deformation of aluminum around the micropores owing to the presence of high hydrogen pressure in the micropores. It has been reported that at least 60% of the micropores are formed heterogeneously on particles. Our earlier study provides little evidence that vacancies are involved in any way in the micropore formation process. In the previous research, an Al-Mg alloy and aluminum with 99.999% purity and with an almost identical total hydrogen content were exposed at 823 K, resulting in a marked difference between them in the number density and size of micropores. This means that heterogeneous nucleation sites appear to be necessary for hydrogen to form micropores. When there are no such sites, micropore formation is

effectively suppressed. A second increase in number density is observed at 807 K in Fig. 11 after 10.8 ks has elapsed. This corresponds well to the observed increase in the number of eutectic regions in Fig. 8. It can be presumed that if particles or eutectic regions acting as nucleation sites are melted due to the high-temperature solution treatment, the overall creep deformation resistance of the surrounding aluminum matrix decreases greatly, and this may induce the rapid growth of the micropores. A combination of stiffer eutectic regions with adjacent micropores might also cause stress concentration around the micropores when the materials are loaded under tension at room temperature.

5.2.3 Fracture paths in tensile tests

Figures 12 and 13 show two representative tomographic images of fractured specimens obtained in tensile tests after solution treatments at 807 K for 7.2 and 10.8 ks, respectively. Only the areas with Cu concentrations higher than 10 % are shown in the figure together with micropores highlighted in blue. In Fig. 12, it seems most likely that the fracture is triggered in a relatively coarse eutectic region with a high Cu concentration located near the specimen surface. Some other small green regions are located on the fracture surface. The part of the fracture surface where these green regions are observed (the nearer side of the fracture surface in Fig. 12) is inclined at an angle of about 40 degrees with respect to the loading axis. The specimen was broken in a brittle manner without any damage initiation in the vicinity of the fracture surface. These observations suggest that the fracture resistance of this plane is weakened considerably by the high density of the eutectic particles shown in Figs. 7 and 8, and as a result the crack passed through this plane. It can be also seen that the green regions remain intact on the fracture surface, suggesting that the crack passed through the eutectic region/aluminum matrix interfaces. In Fig. 13, a crack is seen to trace a few coarse micropores as well as some high Cu regions. The crack path is also tortuous threading through these micropores. Although some eutectic regions are also located on the fracture surface, it can be concluded that in this case the agglomerated coarse micropores triggered the fracture. In these observations, the specimens are too small, owing to the limitations of X-ray transmission, for us to see the general tendency of the fracture behavior through the materials with a single specimen. However, it can be confirmed that these two features act as fatal defects during the fracture.

6. Discussion

The average Cu concentration in the α-Al phase increased from 2.1 mass % in the as-cast condition to 4.5 mass % during the 7.2 ks solution treatment at 807 K where the spatial distribution of the copper becomes completely homogeneous. It is reasonable to assume that the average Cu concentration in the aluminum matrix of the Al-Si eutectic phase is almost identical to that of the α-Al phase after a solution treatment of 7.2 ks at 807 K. Nevertheless, the Vickers hardness value for the whole material was much lower than that for the α-Al phase, and started to decrease earlier than the α-Al phase as a result of the solution treatment at 807 K. This implies that the mechanical properties of the Al-Si eutectic phase would be significantly inferior to those of the α-Al phase even under compressive stress during indentation. Since a pure ternary alloy was used in the present study, the previously reported effects of irregular-shaped intermetallic compound particles other than $CuAl_2$ [4,6] can be excluded in this case. Only two microstructural features; micropores and Al-Si-Cu ternary eutectic particles can be assumed to have a detrimental effect on the mechanical properties after the high-temperature solution treatment. Of these, micropores are assumed to be harmful especially under tension. In addition, the volume fraction, size and number density of the micropores are not significantly different at 807 and 824 K, and almost identical for 7.2 and 10.8 ks at 807 K, where the difference in hardness is more or less observed. It can therefore be concluded that the effects of the micropores are not of primary importance.

On the other hand, irregular-shaped and networking Al-Si-Cu eutectic regions were seen at 824 K together with a correspondingly low Cu content even in the α-Al phase. It can be readily assumed that such a brittle phase with an irregular shape can be fractured even under compression, thereby inducing damage formation. The Al-Si-Cu eutectic phases are almost spherical and relatively small after a solution treatment at 807 K for 10.8 ks. The observed reduction in Vickers hardness might be attributed to the existence of high-density eutectic particles providing a fracture path with a low fracture resistance as shown in Fig. 12. As previously reported [19], there are non-symmetrical stress–strain fields near the crack tip in inhomogeneous materials, which result in a near-tip mixed-mode loading. This in turn induces crack deflection and the fracture path in response to the magnitude and sign of the mode II loading component. It is known that if there is a particle

that is stiffer than the underlying matrix, any crack is always deflected from the particle [20]. On the other hand, if there is a micro-crack or pore, which accelerates the flow of the underlying matrix material, the crack is deflected towards those features, and the features are subsequently absorbed into the crack [20]. This implies that for a fracture path to be realized through the stiff eutectic regions as shown in Fig. 12, these regions must be broken or the interfaces with the matrix debonded before the crack approaches. If not, there should be micropores adjacent to the eutectic regions. Anyway, it can be concluded that the positive effects can outweigh the negative effects even above a eutectic temperature only when the effects of the brittle eutectic regions and neighboring micropores are limited, thereby realizing the maximum strength at a relatively high temperature.

7. Summary

The dual-energy K-edge subtraction imaging technique and the high-resolution synchrotron X-ray microtomography technique have been employed to obtain the spatial distribution of copper and the changes it undergoes during solution treatment. The former technique was effective for examining age-hardenability and its spatial variation, while the latter technique was used to observe the effects of incipient local melting and the accompanying growth of micropores adjacent to the melt regions. It was clarified that the age-hardenability of the α-Al phase increases effectively with increases in solution treatment temperature up to 807 K together with complete homogenization, while that for an aluminum matrix in the Al-Si(-Cu) eutectic phase is suppressed owing to the existence of negative factors such as the formation of coarse and irregular-shaped regions with high Cu concentrations and coarse micropores. It was demonstrated that the strength of the Al-Si-Cu alloy is maximized with a solution treatment at 807 K for 7.2 ks, which is approximately 16 K higher than the ternary eutectic temperature. Complete homogenization was confirmed at this stage in terms of Cu concentration. The sample treated at 824 K exhibited a reduction in Cu concentration together with local variations, while its strength decreased greatly. This is attributable to the instantaneous melting seen at 824 K immediately after the onset of heating. It can be seen that micropore growth accelerated at 807 K or above owing to the melting of adjacent eutectic regions.

A combination of stiffer eutectic regions with adjacent micropores might result in stress concentration around the micropores when the materials are loaded under tension at room temperature. This study has provided visual evidence for both the positive and negative effects exerted on the mechanical properties of an aluminum alloy by a high-temperature solution treatment. We conclude that the positive effects can outweigh the negative effects even above the eutectic temperature. As a result the maximum strength is realized at a relatively high temperature with a significant reduction in the time required for solution treatment.

Acknowledgements

The synchrotron radiation experiments were performed with the approval of JASRI through proposal number 2006B1239, 2007A1431 and 2008A1104. This work was partly undertaken as part of the Grant-in-aid for Scientific Research (A) from the JSPS through subject No. 20246102. One of the authors (HT) is also grateful for the support of the Light Metal Educational Foundation.

References

1) Hatch JE. Aluminum ; properties and physical metallurgy. Materials Park (OH) : ASM International, 1984, p.32-36

2) Reiso O, Ryum N, Strid J. Metall Trans A 1993;24A:2629-2641

3) Droenen PE, Ryum N. Metall Trans A 1994;25A:521-530

4) Shimizu Y, Awano Y, Nakamura M. J Japan Inst Light Met 1988;38:202-207 (in Japanese).

5) Koga M, Ohnishi N, Iizuka Y, Takaai T, Nakayama Y. J Japan Inst Light Met 1993;43:297-302 (in Japanese).

6) Irinouchi Y, Toda H, Sakai T, Kobayashi T, Wang L. J Japan Inst Light Met 2005;55:159-163 (in Japanese).

7) Sokolowski JH, Djurdjevic MB, Kierkus CA, Northwood DO. Journal of Materials Processing Technology 2001;109:174-180.

8) Toda H, Hidaka T, Kobayashi M, Uesugi K, Takeuchi A, Horikawa K. Acta Mater 2009;57:2277-2290

9) Toda H, Minami K, Koyama K, Ichitani K, Kobayashi M, Uesugi K, Suzuki Y. Acta Mater 2009;57: 4391–4403

10) Qian L, Toda H, Uesugi K, Kobayashi M, Kobayashi T. Phys Rev Lett 2008;100:115505

11) Toda H, Yamamoto S, Kobayashi M, Uesugi K. Acta Mater 2008;56:6027-6039

12) Toda H, Shimizu K, Kobayashi M, Uesugi K, Suzuki Y. Acta Mater 2009; to be submitted.

13) Ikeda S, Nakano T, Tsuchiyama A, Uesugi K, Suzuki Y, Nakamura K, Nakashima Y, Yoshida H. American Mineralogist 2004;89:1304-1312

14) Lorensen WE, Cline HE. Computer graphics 1987;21:163-169

15) International Tables for X-Ray Crystallography, Vol.III. Physical and Chemical Tables. In: MacGillavry CH, Rieck GD, editors. Birmingham, England : The Kynoch Press, 1962. p.161.

16) Aluminum, Volume 1: Properties, Physical Metallurgy and Phase Diagrams. In: Van H, Kent R, editors. Materials Park (OH) : ASM International, 1967. p. 364.

17) Mondolfo LF. Aluminum Alloys: Structures and Properties. London : Butterworth, 1979. p.253-278.

18) Silcock JM, Heal TJ, Hardy HK. J Inst Metals 1953-1954;82:239-248

19) Sugimura Y, Lim PG, Shih CF, Suresh S. Acta Metall Mater 1995;43:1157–69

20) Toda H, Kobayashi T, Goda T. Aluminum alloys: Their Physical and Mechanical Properties: Proc. of 6th. International Conference on Aluminum Alloys. In: Sato T, Kumai S, Kobayashi T, Murakami Y, editors. Tokyo : The Japan Institute of Light Metals, 1998. p.1873-1878.

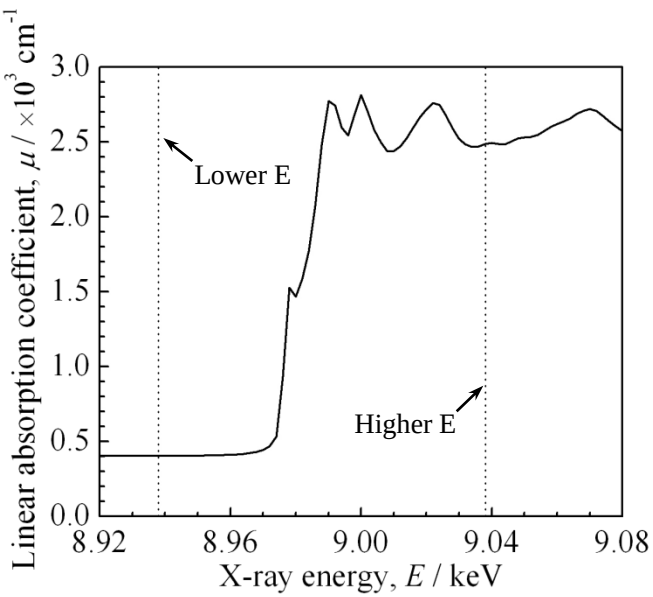

Fig. 1 X-ray absorption spectrum at the copper K-edge of a pure copper film (99.99 %) averaged over the whole beam size of 8 × 0.6 mm.

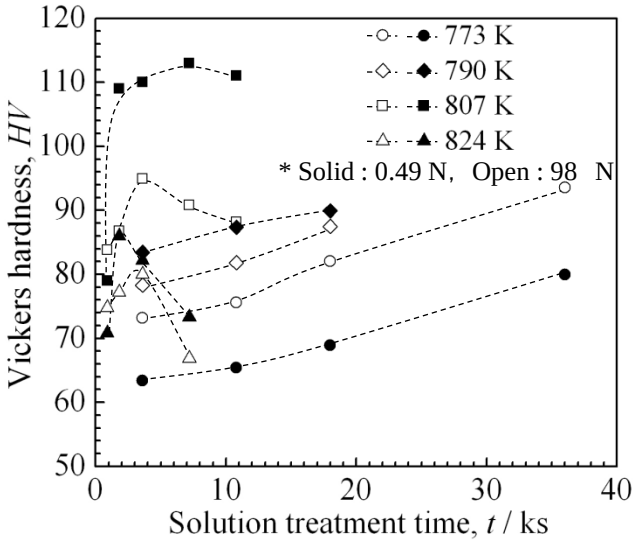

Fig. 2 Relationship between Vickers hardness and heat treatment conditions.

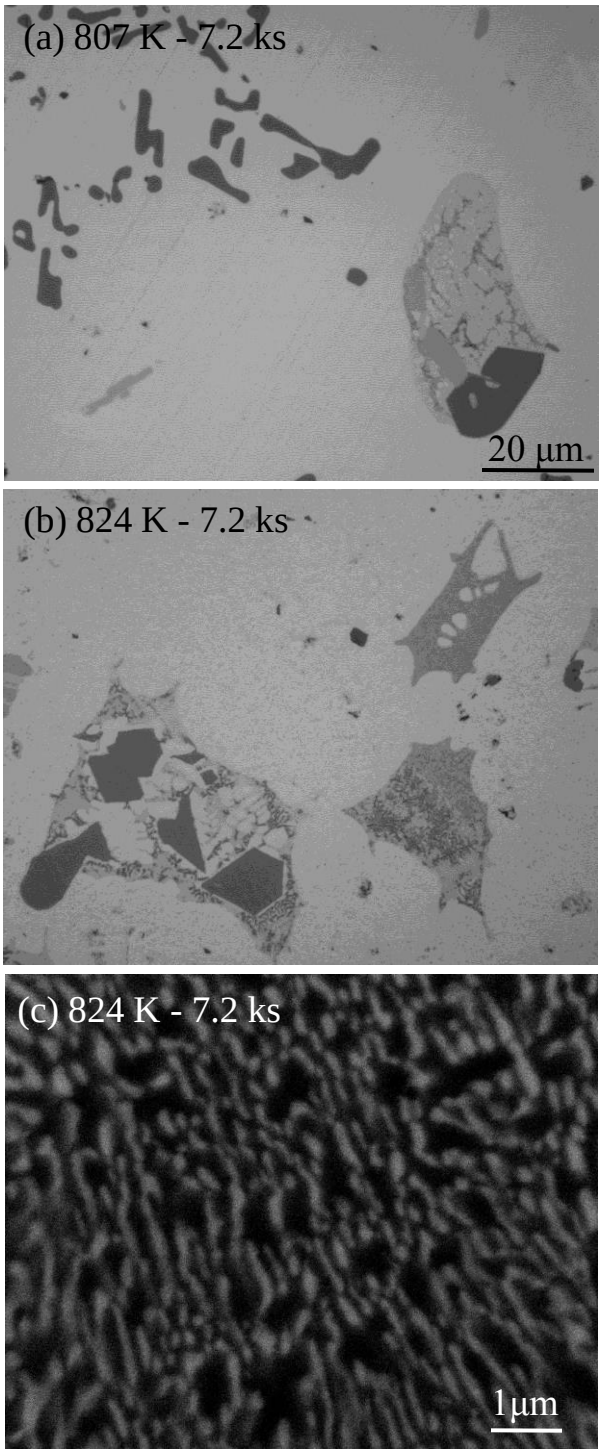

Fig. 3 Optical micrographs taken after an ageing treatment. (a) and (b) were solution heat treated at 807 and 824 K, respectively for 7.2 ks. (c) is a magnified view of the burnt region shown in (b) obtained with a scanning electron microscope.

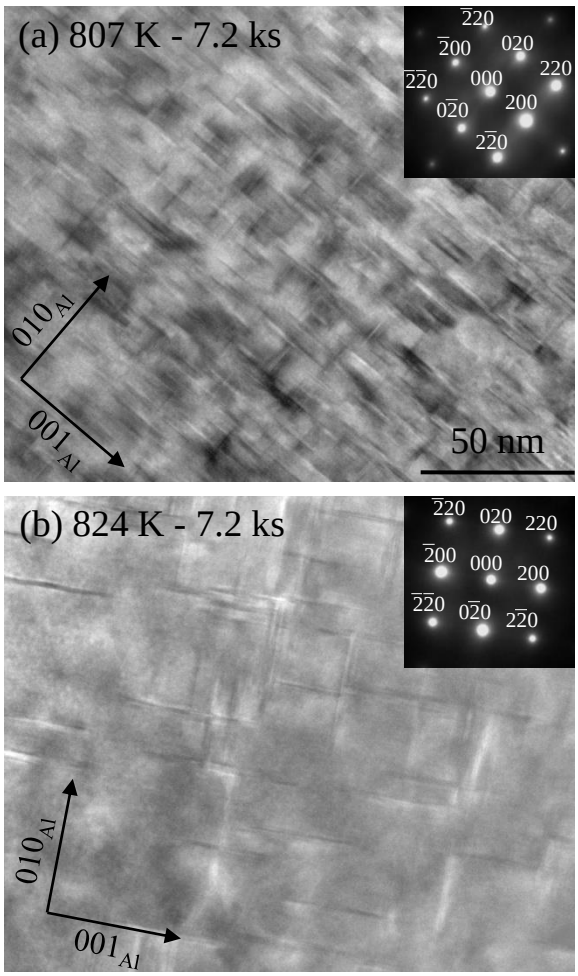

Fig. 4 Bright field TEM micrographs, representing age-hardening precipitates. Ageing treatment was performed at 433K for 18.0 ks,

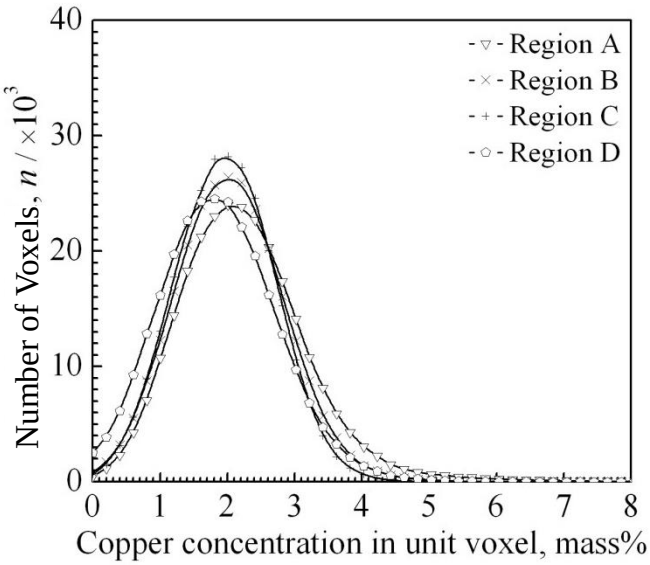

(a) As cast

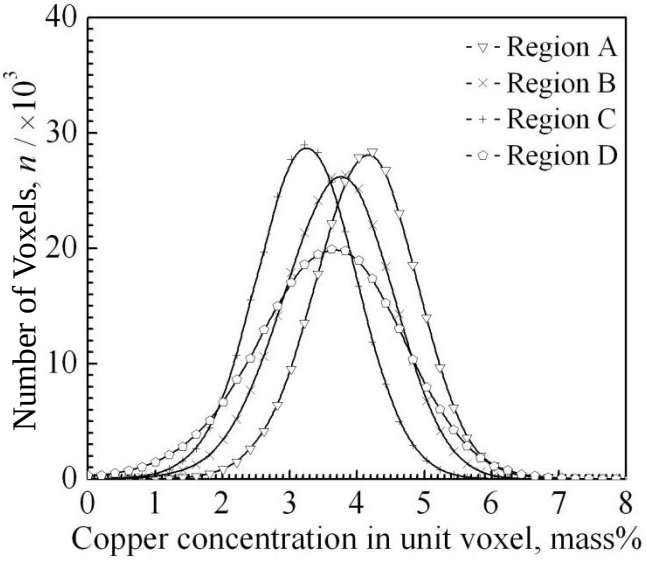

(b) 807 K - 0.9 ks

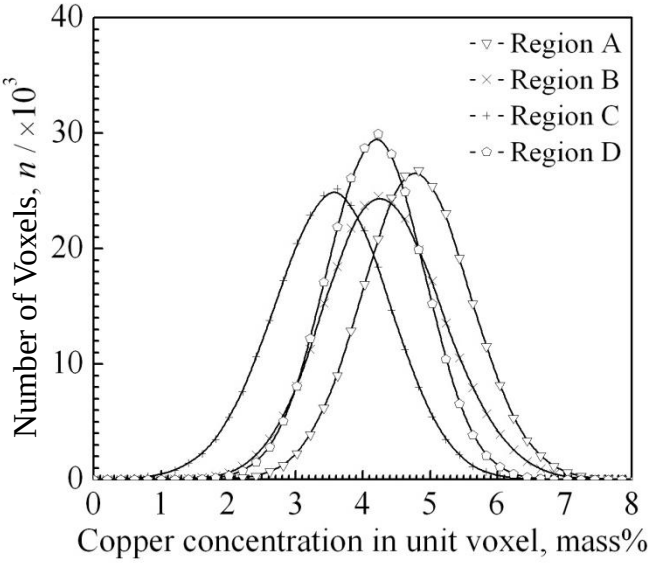

(c) 807 K - 1.8 ks

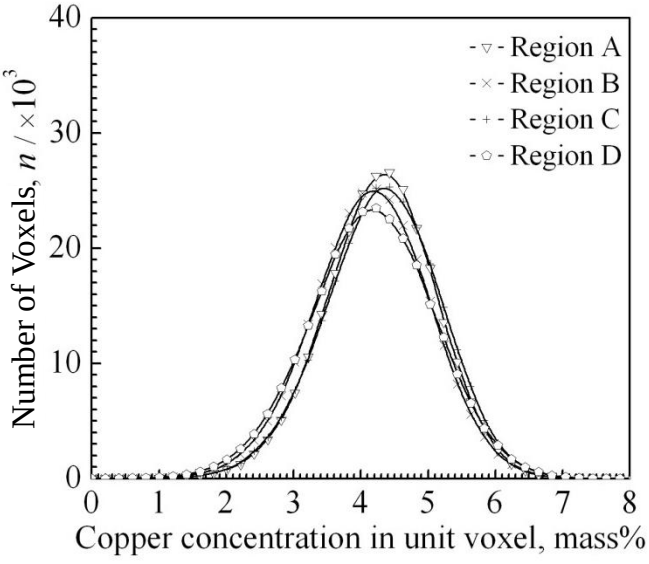

(d) 807 K- 3.6 ks

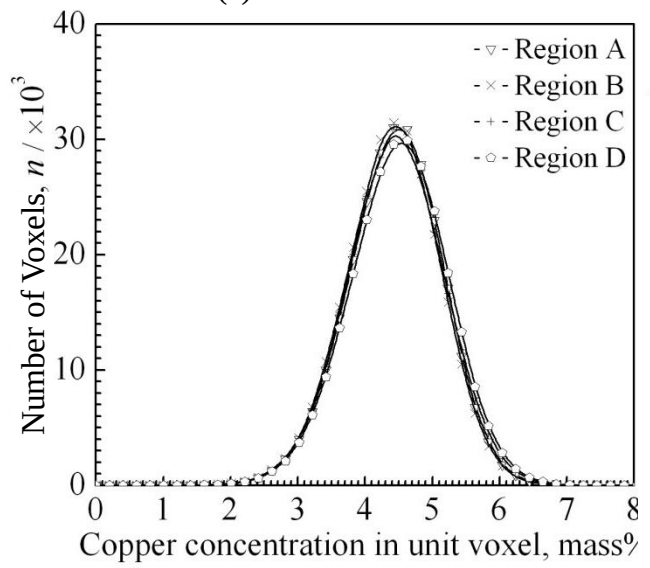

(e) 807 K - 7.2 ks

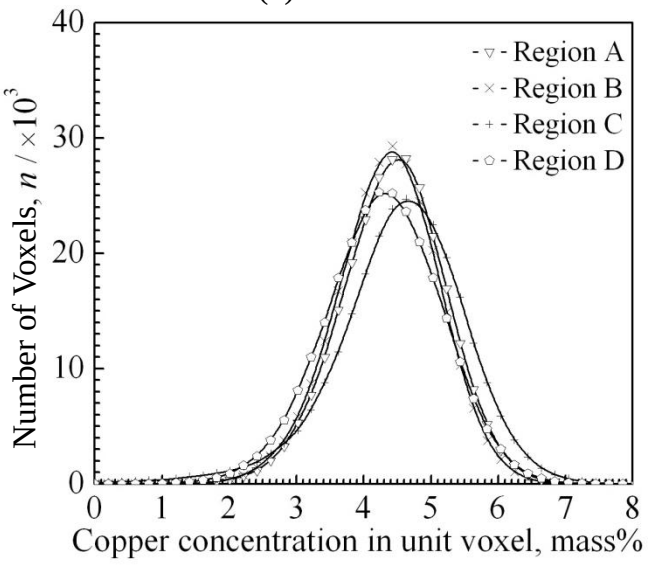

(f) 807 K - 10.8 ks

Fig. 5 Histograms of the local copper concentration in the α-Al phase. The solution treatment temperature was 807 K. Regions A-D are 40 μm in diameter and were extracted so that they were occupied by only the α-Al phase.

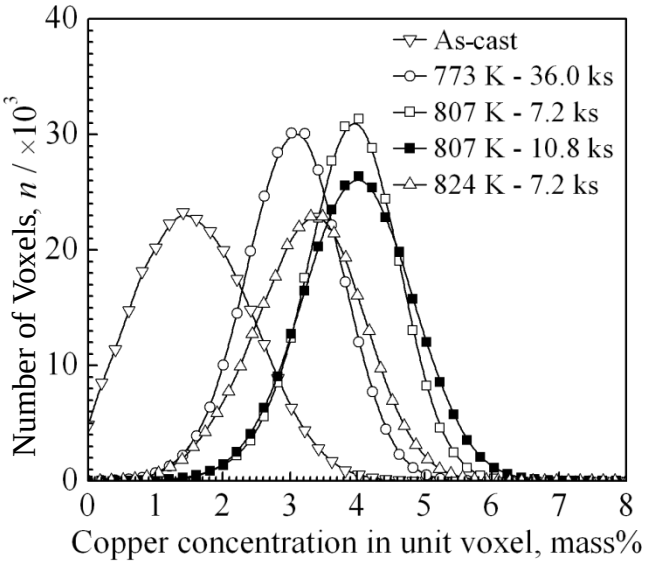

Fig. 6 Histograms of copper concentration for various heat treatment conditions.

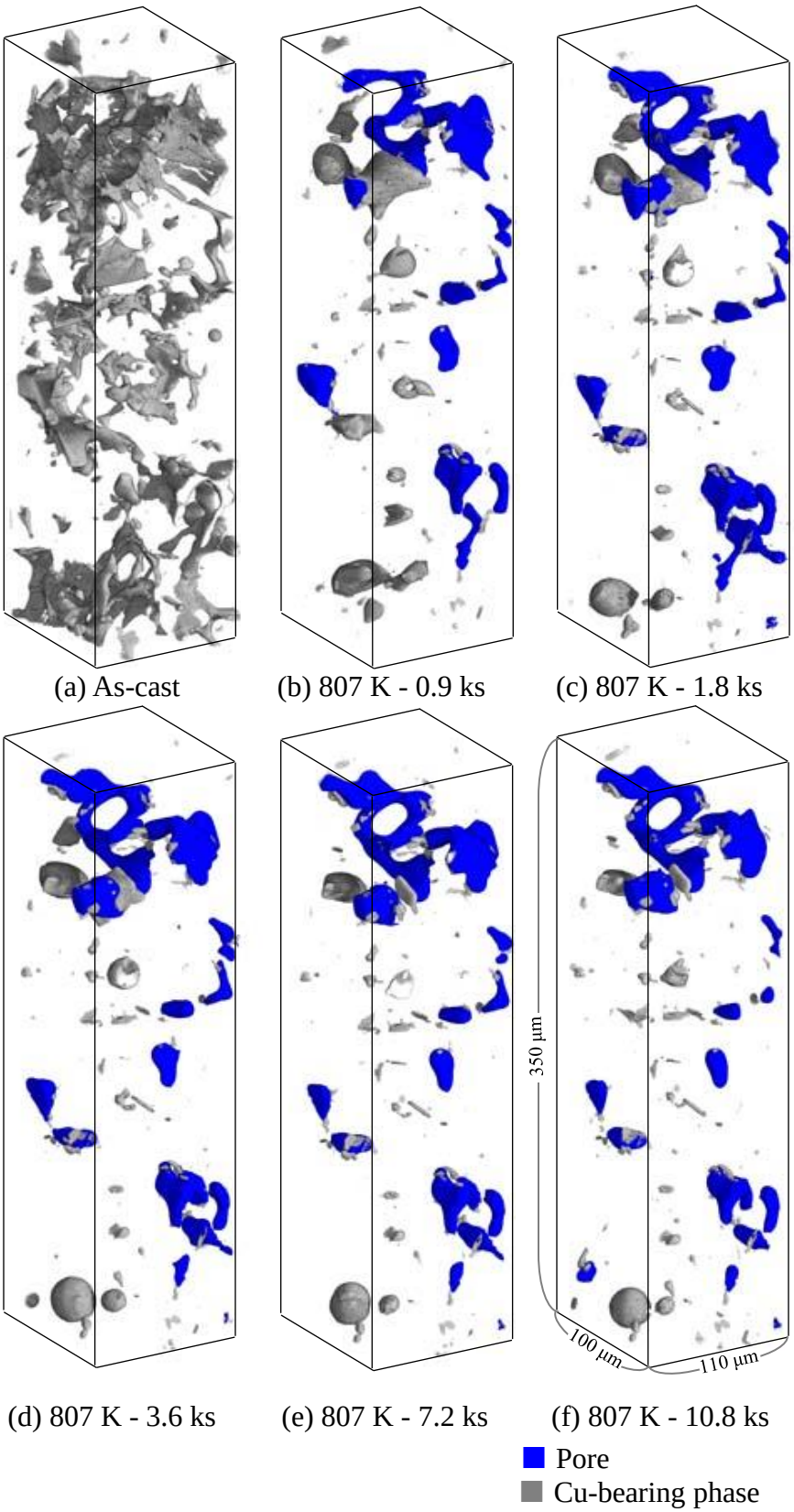

Fig. 7 3-D perspective views of pores and copper-bearing phase. Solution treatment temperature was 807 K.

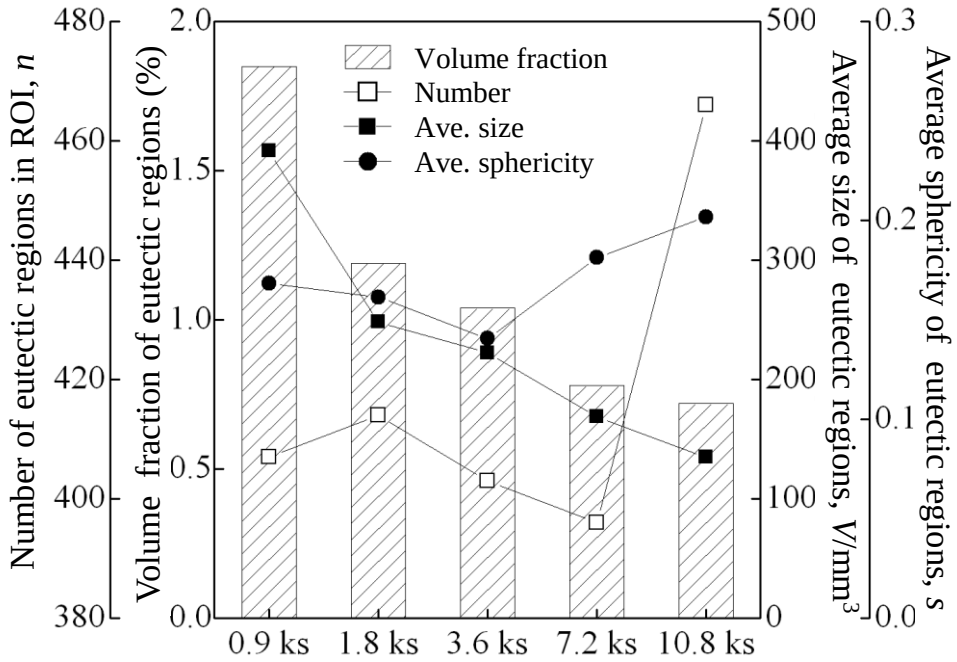

Fig. 8 Variations of volume fraction, number, average size and average sphericity of the copper-bearing phase with solution treatment time at 807 K.

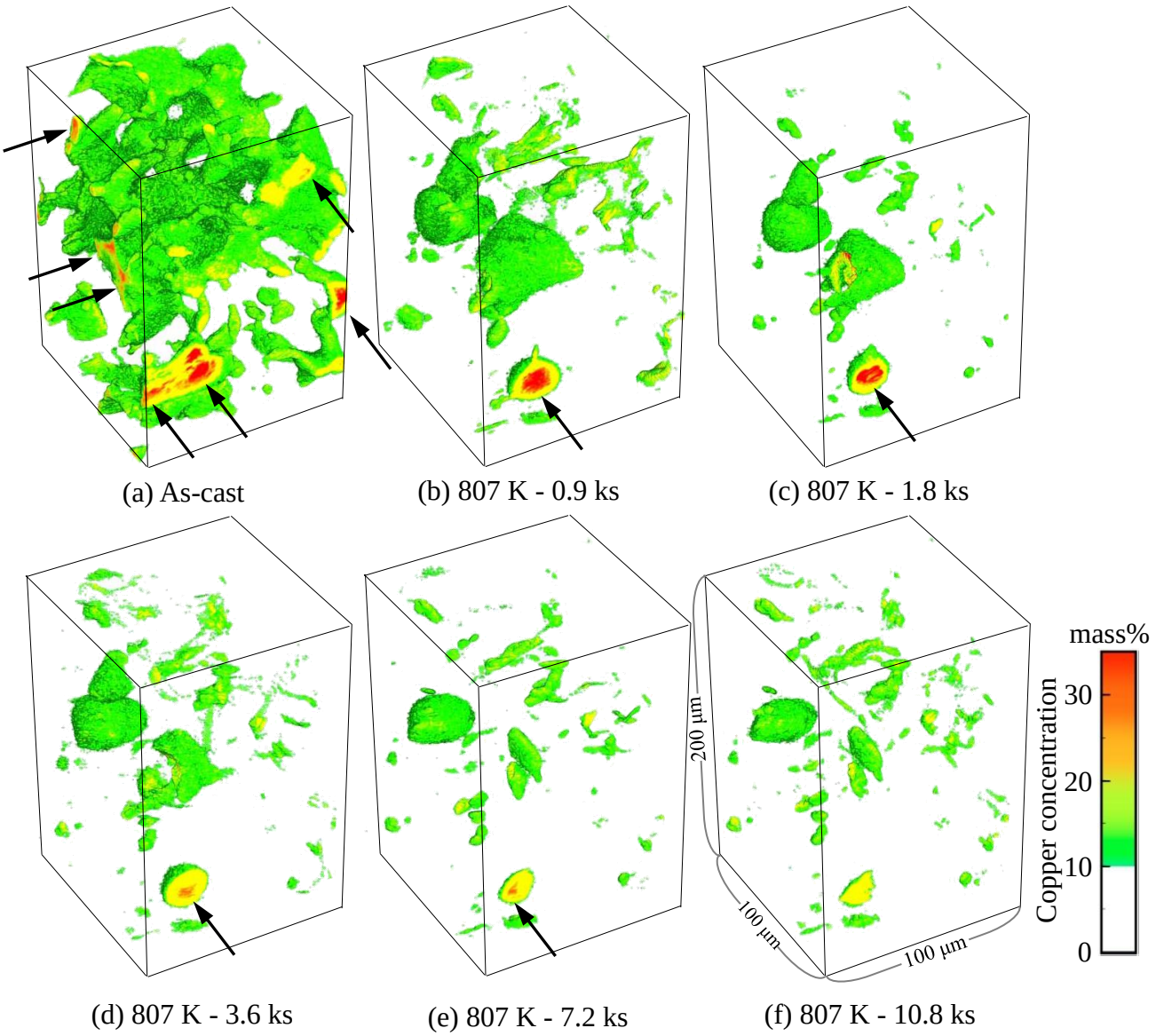

Fig. 9 3-D perspective views of copper-bearing phase in the material shown as the Cu concentration contour. Solution treatment was performed at 807 K for various time periods. Arrows indicate red regions, which indicate Cu concentrations higher than 30 mass %.

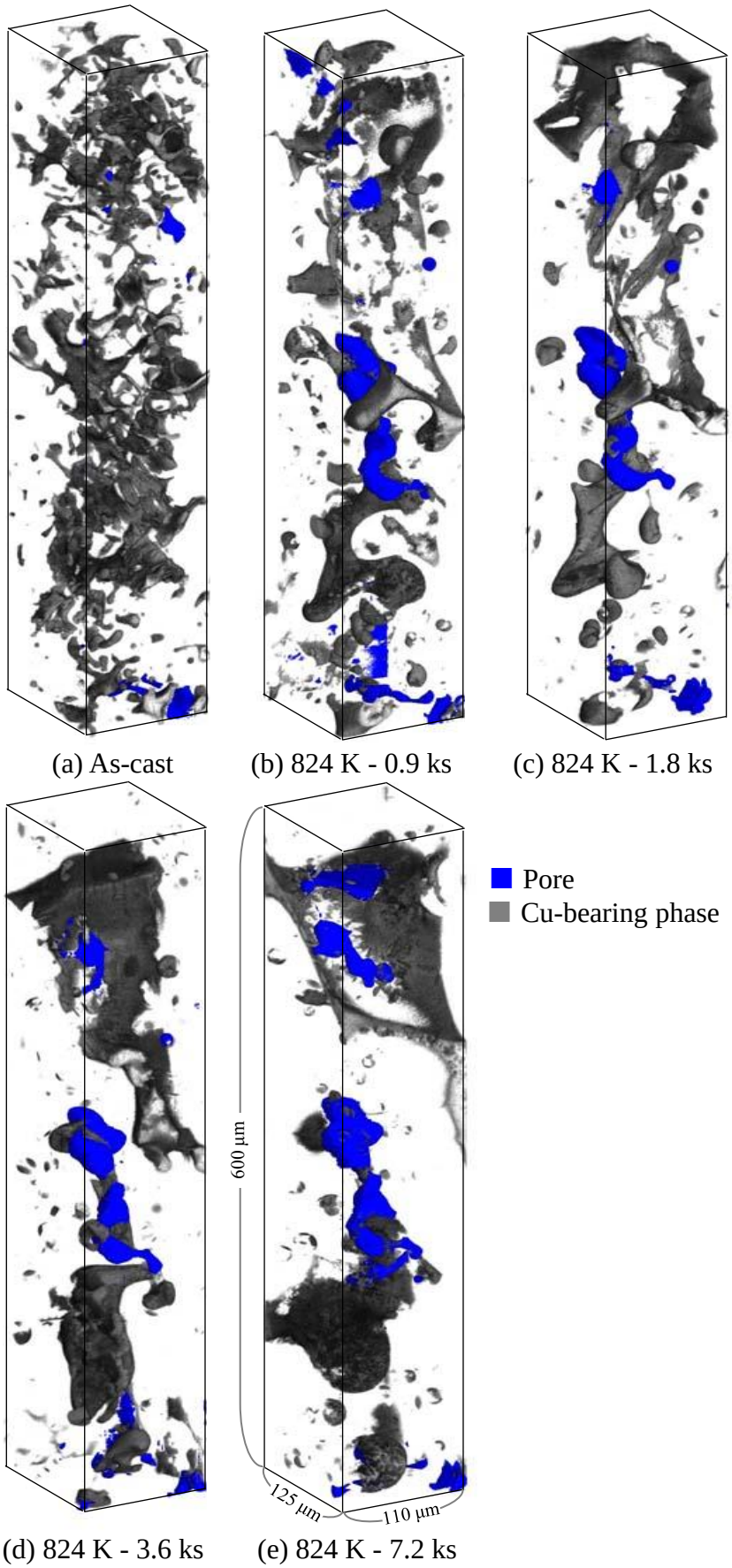

Fig. 10 3-D perspective views of pores and copper-bearing phase. Solution treatment temperature was 824 K.

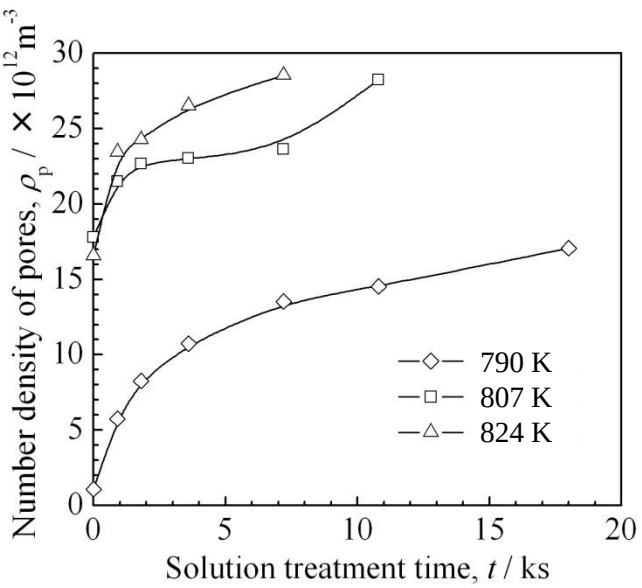

Fig. 11 Variations in number density of micro-pores during solution treatments.

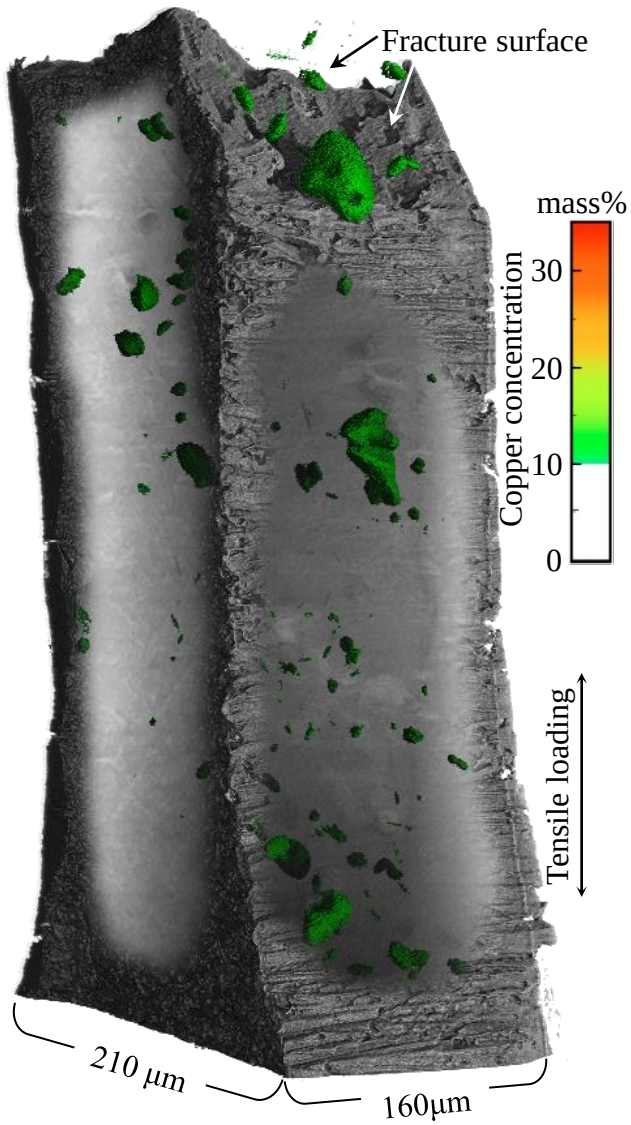

Fig. 12 3-D perspective view of burnt regions with concentration mapping superposed on a fractured specimen image, representing a fracture through the burnt regions. The material was solution-treated at 807 K for 10.8 ks.

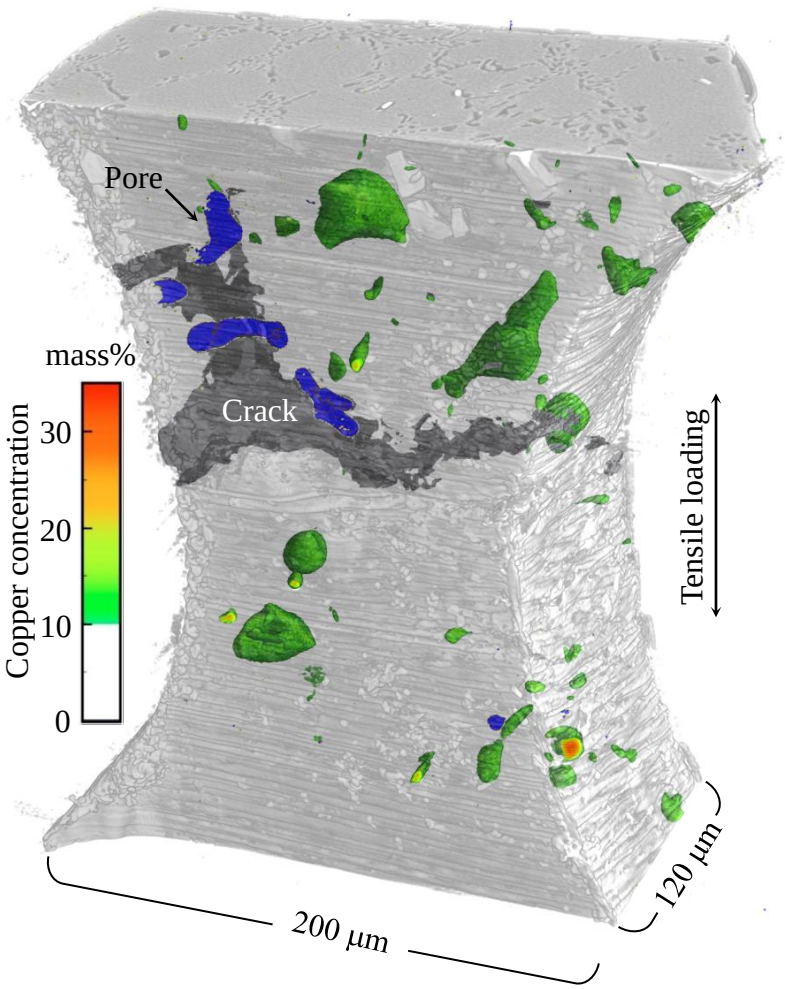

Fig. 13 3-D perspective view of burnt regions with concentration mapping superposed on a fractured specimen image, representing a fracture caused by agglomerated micro-pores. The material was solution-treated at 807 K for 7.2 ks.